

PDRs4AII

IX. Sulfur elemental abundance in the Orion Bar

Asunción Fuente¹, Evelyne Roueff², Franck Le Petit², Jacques Le Bourlot^{2,26}, Emeric Bron², Mark G. Wolfire³, James F. Babb⁴, Pei-Gen Yan⁴, Takashi Onaka⁵, John H. Black⁶, Ilane Schroetter⁷, Dries Van De Putte⁸, Ameek Sidhu^{9,10}, Amélie Canin⁷, Boris Trahin¹¹, Felipe Alarcón¹², Ryan Chown^{9,10}, Olga Kannavou¹¹, Olivier Berné⁷, Emilie Habart¹¹, Els Peeters^{9,10,13}, Javier R. Goicoechea¹⁴, Marion Zannese¹¹, Raphael Meshaka^{11,2}, Yoko Okada¹⁵, Markus Röllig^{16,17}, Romane Le Gal^{18,19}, Dinalva A. Sales²⁰, Maria Elisabetta Palumbo²¹, Giuseppe Antonio Baratta²¹, Suzanne C. Madden²², Naslim Neelamkodan²³, Ziwei E. Zhang²⁴, and P. C. Stancil²⁵

(Affiliations can be found after the references)

Received 13 January 2024 / Accepted 25 March 2024

ABSTRACT

Context. One of the main problems in astrochemistry is determining the amount of sulfur in volatiles and refractories in the interstellar medium. The detection of the main sulfur reservoirs (icy H_2S and atomic gas) has been challenging, and estimates are based on the reliability of models to account for the abundances of species containing less than 1% of the total sulfur. The high sensitivity of the James Webb Space Telescope provides an unprecedented opportunity to estimate the sulfur abundance through the observation of the [S I] 25.249 μ m line.

Aims. Our aim is to determine the amount of sulfur in the ionized and warm molecular phases toward the Orion Bar as a template to investigate sulfur depletion in the transition between the ionized gas and the molecular cloud in HII regions.

Methods. We used the [S III] 18.7 μ m, [S IV] 10.5 μ m, and [S I] 25.249 μ m lines to estimate the amount of sulfur in the ionized and molecular gas along the Orion Bar. For the theoretical part, we used an upgraded version of the Meudon photodissociation region (PDR) code to model the observations. New inelastic collision rates of neutral atomic sulfur with ortho- and para- molecular hydrogen were calculated to predict the line intensities.

Results. The [S III] 18.7 μ m and [S IV] 10.5 μ m lines are detected over the imaged region with a shallow increase (by a factor of 4) toward the HII region. This suggests that their emissions are partially coming from the Orion Veil. We estimate a moderate sulfur depletion, by a factor of ~2, in the ionized gas. The corrugated interface between the molecular and atomic phases gives rise to several edge-on dissociation fronts we refer to as DF1, DF2, and DF3. The [S I] 25.249 μ m line is only detected toward DF2 and DF3, the dissociation fronts located farthest from the HII region. This is the first ever detection of the [S I] 25.249 μ m line in a PDR. The detailed modeling of DF3 using the Meudon PDR code shows that the emission of the [S I] 25.249 μ m line is coming from warm (>40 K) molecular gas located at $A_{\rm V} \sim 1-5$ mag from the ionization front. Moreover, the intensity of the [S I] 25.249 μ m line is only accounted for if we assume the presence of undepleted sulfur.

Conclusions. Our data show that sulfur remains undepleted along the ionic, atomic, and molecular gas in the Orion Bar. This is consistent with recent findings that suggest that sulfur depletion is low in massive star-forming regions because of the interaction of the UV photons coming from the newly formed stars with the interstellar matter.

Key words. astrochemistry – ISM: abundances – HII regions – photon-dominated region (PDR) – ISM: individual objects: Orion Bar

1. Introduction

Gas and solids experience a continuous evolution from their early times in molecular clouds until their incorporation into a growing planet through a protoplanetary disk. Although this evolution lasts for a few million years, we now think that the disk's chemical composition is to a large extent determined by the physical and chemical conditions in the progenitor molecular cloud (see, e.g., Guzmán et al. 2017; Jensen et al. 2019; Booth et al. 2021). Elemental abundances are preserved during the planet formation process, and their values in the progenitor protoplanetary disk will determine the chemical composition of future planet atmospheres. The origin of the raw material needed to facilitate life is not clear, however. The Earth could have

acquired its volatiles and organics from other sources. About 0.5% of the Earth's mass could have come from the bombardment of cometary bodies from the outer Solar System during the so-called Late Veneer (Wang et al. 2013; Ehrenfreund et al. 2015; Caselli 2020). Since the composition of comets seems to be similar to that of the dust grains in the initial protosolar nebula (Capria et al. 2017; Bockelée-Morvan & Biver 2017), we need to follow the whole history of elements in space, from molecular clouds to protoplanetary disks, in order to understand how heavy atoms are incorporated into moons and planets and eventually life-forms.

Sulfur is one of the most abundant elements in the Universe and is known to play a significant role in biological systems in Earth. In the interstellar medium, sulfur is found in gas phase,

Table 1. Studied MIRI lines in order of increasing wavelength with atomic data from NIST (Kramida et al. 2022).

λ (μm)	Species	Transition lower – upper	$A_{ij} \ (\mathrm{s}^{-1})$	E _u (K)
10.5105	[S IV]	$^{2}P_{1/2}^{o} - ^{2}P_{3/2}^{o}$	7.74×10^{-3}	1368.9
17.0348	$H_2 v = 0$	J = 1 - J = 3	4.76×10^{-10}	1015.1
18.7129	[S III]	$^{3}P_{1} - ^{3}P_{2}$	2.06×10^{-3}	1198.7
25.2490	[S I]	${}^{3}P_{2} - {}^{3}P_{1}$	1.40×10^{-3}	569.83

Notes. Line parameters of the H₂ line are from Roueff et al. (2019).

in interstellar ices, and in the refractory material that eventually can form terrestrial planets. The elemental abundances defined as the fraction of a given element in volatiles (gas + ice) are essential parameters for understanding the chemistry of interstellar gas and the composition of the refractory grain cores. However, while the carbon and oxygen budgets in star-forming regions have been extensively studied, there are still a lot of open questions regarding the amount of sulfur and its relative distribution between volatiles and refractories in the interstellar medium. Observations in diffuse clouds are consistent with essentially undepleted sulfur (Sofia et al. 1994; Neufeld et al. 2015). Moderate sulfur depletions (by less than a factor of 10) are also consistent with observations of sulfur-bearing species in some photodissociation regions (PDRs; Goicoechea et al. 2006, 2021; Goicoechea & Cuadrado 2021). However, the sum of the observed abundances of sulfur molecules in gas and ice only constitutes <5% of the expected amount in cold regions (Vastel et al. 2018; Rivière-Marichalar et al. 2019; Fuente et al. 2019), and sulfur depletion seems to be larger than a factor of ~10 in the shielded and densest regions of dark clouds based on model analyses (see, e.g., L1544: Hily-Blant et al. 2022; Fuente et al. 2023). The given evolutionary stage at which this big depletion occurs and the form in which sulfur is incorporated into (semi-)refractory material is still unknown. For instance, it has been suggested that the so-called depleted sulfur might be locked in refractory FeS (Kama et al. 2019). Sulfur could also form semi-refractory material such as sulfur allotropes (Jiménez-Escobar & Muñoz Caro 2011; Jiménez-Escobar et al. 2012; Fuente et al. 2019; Shingledecker et al. 2020; Cazaux et al. 2022). Different sulfur reservoirs would translate into different fractions of sulfur in volatiles in protoplanetary disks, which would lead to different compositions of planets and paths for sulfur leading to life. Understanding the details of sulfur depletion is therefore an essential question in astronomy.

Chemical models predict that 88% of the sulfur in cold molecular clouds ($n_{\rm H} = 2 \times 10^4 \ {\rm cm}^{-3}$, $T = 10 \ {\rm K}$) is in atomic form at a typical age of 0.1 Myr (see, e.g., Vidal et al. 2017). However, due to its high excitation conditions (see Table 1), the [S I] 25.249 µm line has only been detected in bipolar outflows (Anderson et al. 2013) thus far, precluding accurate knowledge of its abundance in most environments and the full testing of our chemical models. PDRs are regions where most of the gas is neutral (i.e., H or H₂) and their physical and chemical conditions are determined by far-ultraviolet (FUV) photons (i.e., 6 eV < E < 13.6 eV) emitted by massive stars. PDRs are found in essentially all relevant astrophysical environments, including diffuse clouds, protoplanetary disks, molecular cloud surfaces, globules, planetary nebulae, and starburst galaxies. Investigating sulfur chemistry in PDRs is of paramount importance to disentangling the problem of missing sulfur since PDRs constitute the transition between the sulfur undepleted ionized gas and the heavily depleted molecular cold gas.

The James Webb Space Telescope (JWST; Gardner et al. 2006) Early Release Science (ERS) program "PDRs4All: Radiative feedback from massive stars" has observed the prototypical PDR usually referred to as the Orion Bar as a template for the study of Galactic and extragalactic PDRs (Berné et al. 2022). The Orion Bar is the sharp edge bordering the HII region M 42, which is located on the near side of the giant molecular cloud OMC 1, at a distance $D = 414 \pm 7$ pc. (Menten et al. 2007). Observations of this so-called Orion Bar in radio-continuum, vibrationally excited H₂ (Hayashi et al. 1985) and at 3.3 μm (Bregman et al. 1994) show that the bar is formed by the gas associated with an almost edge-on ionization front (IF). Because of this favorable geometry and its closeness to the Solar System, the Orion Bar is probably the best studied PDR and an ideal test bench for chemical models. The gas associated with the Orion Bar has been widely studied at all wavelengths (Omodaka et al. 1994; Tauber et al. 1994, 1995; Hogerheijde et al. 1995; White & Sandell 1995; Fuente et al. 1996, 2003). Burton et al. (1990) modeled the Orion Bar with a density $n_{\rm H} = 10^5~{\rm cm}^{-3}$ and an UV intensity field of $\sim 1 \times 10^5$ in Habing field units using available near- and mid-infrared observations (Hayashi et al. 1985; Peimbert & Torres-Peimbert 1977; Haas et al. 1986). Based on *Herschel* data, Goicoechea et al. (2011) and Joblin et al. (2018) conclude that the emission of the OH and CO far-infrared lines can only originate from small structures with typical thicknesses of a few times 10⁻³ pc and at high thermal pressures ($P_{\rm th} \sim 10^8 \ {\rm K \ cm^{-3}}$). PDRs4All data have provided, for the first time, the possibility to resolve the IF and photodissociation fronts (DFs) in the Orion Bar (Habart et al. 2024; Peeters et al. 2024; Chown et al. 2024). We now know that the Orion Bar is not a single edge-on PDR but a series of edge-on and face-on PDRs formed in the corrugated surface of the molecular cloud surrounding the HII region M 42 (see the sketch in Fig. 1).

This paper aims to characterize the sulfur chemistry in the ionized and warm molecular gas associated with the Orion Bar to eventually determine the sulfur depletion along the border of the molecular cloud. The [S IV] 10.5 μm and [S III] 18.7 μm lines are used to trace the ionized gas, and a comparison of the H_2 S(1) and [S I] 25.249 μm lines allows us to determine sulfur depletion in the molecular phase. Combining these results with previous estimates of the sulfur abundance in the M 42 nebula using optical lines (Esteban et al. 2004; Daflon et al. 2009) and the estimation in the S+/S transition region using the sulfur recombination lines from Goicoechea & Cuadrado (2021), we are able to determine the amount of sulfur in all the gaseous phases across the Orion Bar.

2. Observations

This paper is based on observations of the ERS program "PDRs4All: Radiative feedback from massive stars" (ID1288¹), PIs: Berné, Habart, Peeters; Berné et al. 2022). Within this program, the Orion Bar PDR has been observed with NIRSpec and the Mid-Infrared Instrument (MIRI) in medium resolution spectroscopy (MRS) mode (Wells et al. 2015; Argyriou et al. 2023). MIRI observations were performed over a 1 × 9 pointing mosaic, which defines a rectangle almost perpendicular to the Orion Bar (see Fig. 1 and Chown et al. 2024). This region was observed

¹ pdrs4all.org; https://www.stsci.edu/jwst/scienceexecution/program-information.html?id=1288

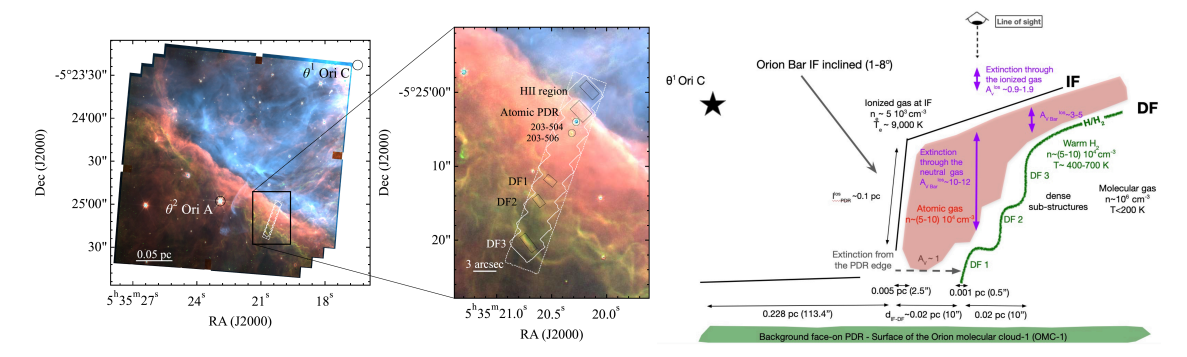


Fig. 1. Overview of the NIRSpec and MIRI MRS mosaics observed in PDRs4All and scheme of the geometry of the Orion Bar. Left panel: composite NIRCam image encoded as follows: F335M (AIB emission) in red, F470N-F480M (H₂ emission) in green, and F187N (Paschen α emission) in blue (Habart et al. 2024; Peeters et al. 2024). The footprints of the NIRSpec and MIRI MRS mosaics are shown as solid and dashed lines, respectively. The positions of DF1, DF2, and DF3, as defined by Habart et al. (2024), together with those of the protostars d203-504 and d203-506 are indicated. This figure has been taken from Chown et al. (2024). Right panel: sketch of the Orion Bar adapted from Habart et al. (2024) and Peeters et al. (2024).

in all four MRS channels (channels 1, 2, 3, and 4), and all three sub-bands within each channel (short, medium, and long). Our resulting 3D maps cover the full MRS wavelength range (4.90 to 27.90 μm) with a spectral resolution ranging from $R\sim3700$ in channel 1 to $\sim\!1700$ in channel 4 and a spatial resolution of 0.207" at short wavelengths to 0.803" at long wavelengths, corresponding to 86 and 332 AU, respectively at the distance of the Orion Nebula. This paper is focused on the study of the H_2 S(1) 17.035 μm , [S IV] 10.5 μm , [S III] 18.7 μm , and [S I] 25.249 μm lines, all placed in channel 4.

The MIRI/MRS observations were processed from uncalibrated data through the official pipeline, using 1.12.5 of the jwst Python package, with the jwst_1147.pmap Calibration Reference Data System (CRDS) context. We made additional corrections after the default pipeline to improve the quality of our dataset. A detailed description of all these modifications can be found in Van De Putte et al. (2024). In current data cubes, the wavelength calibration is accurate up to a few km s⁻¹ at short wavelengths, and about 30 km s⁻¹ at the longest wavelength (Argyriou et al. 2023). The pointing accuracy is about 0.45" without target acquisition, and the typical accuracy of the assigned coordinate system is about 0.3", where the main source of uncertainty is the guide star catalog (Patapis et al. 2024). The spectrophotometric calibration was initially based on a single standard star (Gordon et al. 2022), but data from additional stars were recently introduced into the calibration. The inclusion of these additional calibration data (since jwst_1094.pmap), led to an improved matching of the continuum flux between the four channels of MIRI/MRS, with only minor flux offsets in the overlap regions between the channels (Van De Putte et al. 2024). Together with support for time-dependent calibrations, this postprocessing much improved the continuum flux and calibration of channel 4 where our lines are found. This improvement was specially important in the case of the weaker [S I] 25.249 µm line. As reported in the JWST user documentation², there may remain a 10% systematic uncertainty in the calibration.

3. Results

Figure 2 shows the peak intensity maps of the lines in Table 1. We selected the H_2 S(1) line to complete our study because it

is located in channel 4 and presents similar excitation conditions and angular resolution as the sulfur lines relevant for this work. The high excitation rotational H₂ lines will be presented elsewhere (Sidhu et al., in prep.). For reference, the positions HII, Atomic, DF1, DF2, and DF3 as defined by Peeters et al. (2024) are indicated with crosses in all panels. The coordinates of these positions are listed in Table A.1. The positions of the protoplanetary disks d203-504 and d203-506 (Bally et al. 2000) are also marked with empty circles. Different spatial distributions are observed according with the expected chemical and physical structure produced by the UV radiation impinging in the molecular cloud. The emission of the [S IV] 10.5 µm and [S III] 18.7 µm lines extends over all the mapped area with their intensities increasing by a factor of ~4 toward HII. This spatial distribution is consistent with previous Spitzer observations reported by Rubin et al. (2011) who showed that the emission of these lines extends to more than 10' SW from Θ^1 Ori C. These authors interpreted this extended emission as coming from the fainter outer nebula usually called the Orion Veil (Abel et al. 2004, 2006). The emission of the H₂ S(1) line probes the warm molecular gas associated with the PDR formed between the interface between the HII region and the molecular cloud. This is a corrugated interface, which produces a series of bright H2 S(1) rims (edgeon PDRs) emerging from an extended weaker emission (face-on PDRs; Habart et al. 2024; Peeters et al. 2024). The three brightest ridges are associated with the positions DF1, DF2, and DF3 (see Fig. 2). Weak H₂ S(1) emission coming from the face-on part of the PDR is detected in the region between these DFs, especially between DF2 and DF3. The emission of the [S I] 25.249 μm line is weak and remains undetected toward HII, Atomic, and DF1. It is detected toward DF2 and DF3, and its emission remains high between them. In fact, its intensity smoothly increases beyond DF1 until DF3 in the mapped area (see Fig. 2).

In Fig. 3, we show the normalized emission of the [S IV] 10.5 μm , [S III] 18.7 μm , [S I] 25.249 μm , and H_2 S(1) lines along the cut shown in Fig. 2. The emission of the [S IV] 10.5 μm and [S III] 18.7 μm lines increases toward the HII region. The H_2 S(1) line is detected from the HII region to the molecular cloud, with peaks close to DF1, DF2, and DF3. A different distribution is observed in the [S I] 25.249 μm line whose emission smoothly increases toward the molecular cloud. Contrary to H_2 S(1), the emission of [S I] 25.249 μm remains high beyond DF3. This suggests that at least part of gas emitting in the [S I] 25.249 μm

https://jwst-docs.stsci.edu/jwst-calibrationpipeline-caveats/jwst-miri-mrs-pipeline-caveats

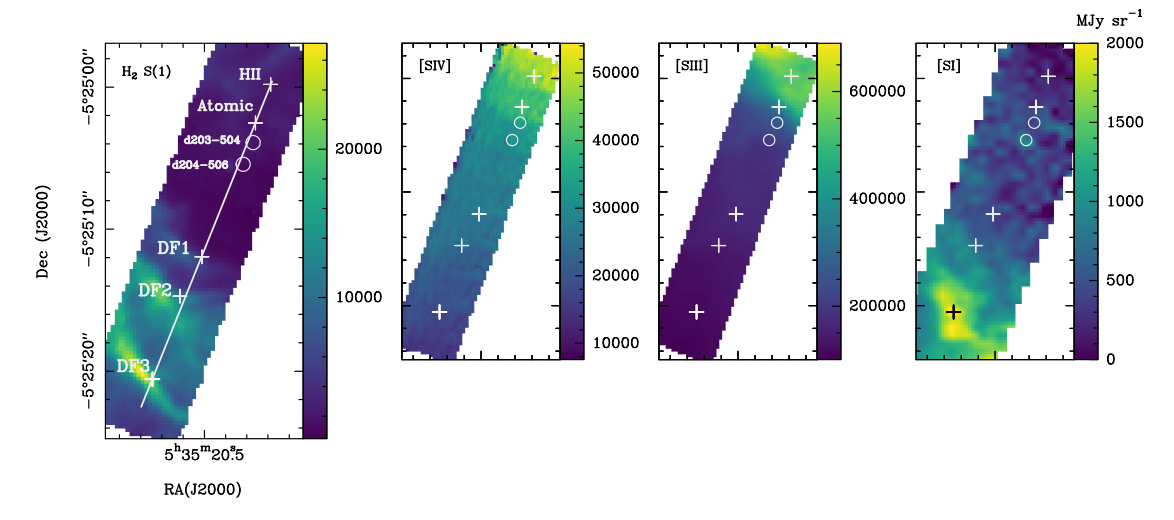


Fig. 2. Peak intensity maps of the lines indicated in the top-left corner of each panel. All the maps have been re-grided to a pixel of \sim 0.3". Crosses indicate the positions of HII, Atomic, DF1, DF2, and DF3, as listed in Table A.1. Circles indicate the positions of the protoplanetary disks d203-504 and d203-506 (Bally et al. 2000). The straight line indicates the cut shown in Fig. 3. The rms in each map is: 80 MJy sr⁻¹ (H₂ S(1)), 50 MJy sr⁻¹ ([S III]), and 273 MJy sr⁻¹ ([S I]).

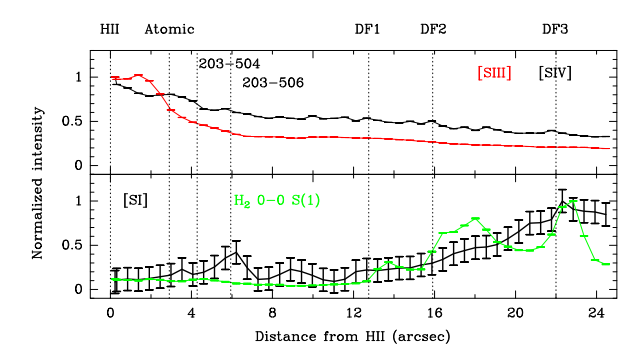


Fig. 3. Cuts along the straight line starting at HII and crossing all the DFs drawn in the $\rm H_2$ S(1) panel of Fig. 2. In all cases, the intensity has been normalized to 1. Dashed lines indicate the positions of HII, Atomic, DF1, DF2, DF3, and the protostellar objects d203–504 and d203–506.

line is located deeper into the molecular cloud than that emitting in the H_2 S(1) line.

Two protoplanetary disks are present in our MIRI-MRS field of view: [BOM2000] d203-504, and [BOM2000] d203-506 (Bally et al. 2000). These disks are well detected in JWST NIR-Cam (Habart et al. 2024; Berné et al. 2024), NIRSpec (Peeters et al. 2024; Berné et al. 2024), and MIRI-MRS (Berné et al. 2023; Zannese et al. 2024). There is no hint of detection of the [S I] 25.249 µm line toward d203-504. A weak peak at ~25.249 μ m at the level of ~2 × rms is found in the cut shown in Fig. 3 at the location of d203-506. In order to search more carefully for the [S I] 25.249 µm line in d203-506, we extracted the MIRI spectrum specifically for this source. We followed the method of Berné et al. (2023), using an elliptical aperture fitted to the size of the source and the subtraction of a background nebular spectrum. The on-source spectrum is extracted from an ellipse centered on d203-506 at the position $\alpha = 5:35:20.357$, $\delta = -5.25.05.81$ with dimensions l = 0.52'', h = 0.38'' and

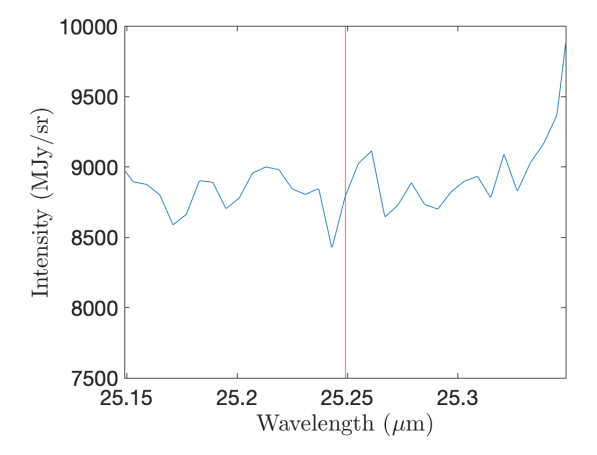


Fig. 4. Spectrum of the d203-506 protoplanetary disk. The red line shows the wavelength of the [SI] line at 25.249 μm . A small feature at \sim 25.257 μm is present but has an intensity lower than $2 \times rms$, precluding any firm detection.

a position angle PA=+33 degrees (trigonometric) with respect to north. The background nebular spectrum is taken at $\alpha=5:35:20.370,\,\delta=-5:25:04.97$ using a circular aperture of radius r=0.365''. The spectrum of d203-506 is obtained by subtracting the background spectrum from the on-source spectrum. This spectrum is shown in Fig. 4. Although there is a slight excess of emission around ~25.257 μm in the spectrum toward d203-506, this excess is lower than 2 × rms and hence we cannot confirm a detection. Therefore, we can only provide an upper limit of $\leq 2.25 \times 10^{-5}$ erg s $^{-1}$ cm $^{-2}$ sr $^{-1}$ for the emission of the [S I] 25.249 μm line toward d203-506, which would imply I ([S I] 25.249 μm) $I(H_2~S(1)) \leq 0.13$ in this silhouette disk using the data from Berné et al. (2023) for I(H $_2~S(1)$). A detailed analysis of the NIRSpec and MIRI spectroscopic data on this object will be the subject of a future paper.

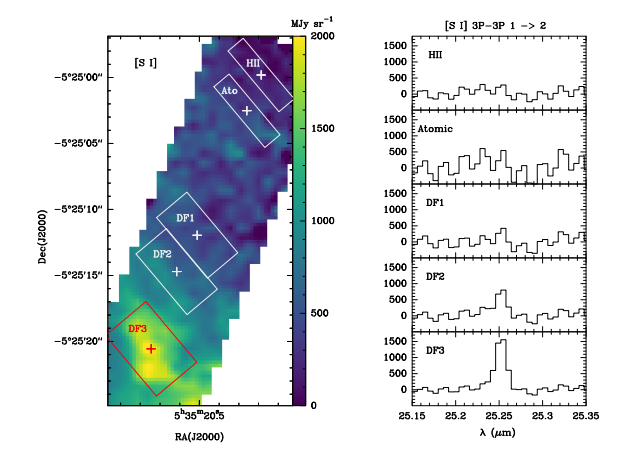


Fig. 5. Spectra of the [S I] 25.249 μm line in the Orion Bar. Left panel: peak intensity map of the [S I] 25.249 μm line. We have drawn the rectangles used to extract the average intensity spectra. Right panel: average intensity spectra of the [S I] 25.249 μm line in the rectangles shown in the left panel.

4. Correction for extinction

We extracted the average spectrum over five rectangular fields centered on the positions HII, Atomic, DF1, DF2, and DF3. The sizes and inclination angle of these rectangles are listed in Table A.1 and the obtained spectra are shown in Figs. 5 and A.1. The integrated line intensities obtained from these spectra are shown in Table A.2. These intensities need to be corrected for the extinction between the gas emitting layer and the observer (A_V^{los}) to obtain the emitted values. For that, we used the expression

$$F_{\rm corr} = F_{\rm obs} \times \exp(\tau_{\lambda}),\tag{1}$$

where $\tau_{\lambda} = N_{\rm H} \cdot \kappa_{\rm abs}$, with $\kappa_{\rm abs}$ being the dust absorption coefficient per hydrogen nuclei. The value of $N_{\rm H}$ can be estimated from $A_{\rm V}^{\rm los}$ using $N_{\rm H}/A_{\rm V}^{\rm los}$ =1.87 × 10²¹ cm⁻² mag⁻¹ according to Joblin et al. (2018). The values of $A_{\rm V}^{\rm los}$ and $\kappa_{\rm abs}$ suffer from large uncertainties. The extinction between the emitting gas and the observer depends on the frequency and the projected distance from Θ^1 Ori C (see the scheme in Fig. 1). Peeters et al. (2024) derived the extinction in the ionized gas using the H I recombination lines. They referred to this value as A_V (foreground) (see Table A.1) and we used it as $A_{\rm v}^{\rm los}$ for the extinction correction of the ions emission. The visual extinction produced by the molecular bar was estimated by the same authors using the H₂ ro-vibrational near-infrared lines and two different assumptions: (i) the dust responsible for the visual extinction is in front of the H_2 emitting layer $(A_V (bar)^1$ in Table A.1); and (ii) the intermingled formalism, which assumes that the dust is mixed with the gas emitting in the H_2 lines (see A_V (bar)² in Table A.1). Since these assumptions correspond to two limiting cases, A_V $(bar)^1$ and A_V $(bar)^2$ can be considered as lower and upper limits to the visual extinction produced by the molecular bar. As discussed in Sect. 3, the emission of the [S I] 25.249 µm line comes from the molecular gas. Accordingly, we estimated lower and upper limits to the H₂ S(1) and [S I] 25.249 μ m extinction-corrected intensities using $A_{\rm V}^{\rm los} = A_{\rm V}$ (foreground) $+A_{\rm V}$ (bar)¹ and $A_V^{los} = A_V$ (foreground)+ A_V (bar)² (see Table A.3). To calculate κ_{abs} , we used the dust opacities tabulated by

Ossenkopf & Henning (1994) for bare grains, Mathis distribution, and assumed dust-to-gas ratio of 0.01. The line intensities thus corrected are shown in Table A.3 and are the ones used to compare with our models. The correction for extinction is less than 33% for the $\rm H_2$ S (1) and [S I] 25.249 μm lines in all fields. Therefore, we do not expect that the uncertainties in $A_V^{\rm los}$ and the optical dust properties have a significant impact in our conclusions.

5. Sulfur abundance in the ionized gas

As noted in Sect. 3, the emissions of the [S III] 18.71 μm and [S IV] 10.51 μm lines extend over several arcminutes further from the IF. Both the extension and the emission profiles of the sulfur ionized lines can be explained if a significant fraction of their emissions come from the fainter foreground ionized gas. This conclusion is confirmed by the *Spitzer* data reported by Rubin et al. (2011), who detected emission of the [S III] 18.71 μm and [S IV] 10.51 μm lines at distances of more than 10' from Θ^1 Ori C. In the following, we estimate the S/H ratio in HII, Atomic, DF1, and DF2 fields based on JWST data and previous optical and near-infrared observations.

The S/H ratio in the ionized gas is calculated by adding up the amount of S³⁺, S⁺⁺ and S⁺ along the line of sight and comparing it with the amount of atomic hydrogen as derived from the Pfund $7\rightarrow 5$ recombination line at $4.654 \,\mu m$ (also called Pf β) taken from Peeters et al. (2024). In order to estimate each species (H+, S++, S3+) column density, we needed to calculate the line emissivities per particle along the line of sight (hereafter, $E_{\rm em}$). The emissivity of each line can be calculated as $E_{\rm em} = f_u \times E_u \times A_{ij}$, where f_u is the fraction of ion density in the upper level, and E_u and A_{ij} are the upper level energy and the Einstein spontaneous emission coefficient, respectively. We obtained the physical conditions in our reference fields from the images of T_e and n_e derived from [S III] 6312 Å/9069 Å and [SII] 6731 Å/6716 Å line ratios by Weilbacher et al. (2015. Figs. 5 and 6 of this paper). Storey & Hummer (1995) tabulated the Pfund $7\rightarrow 5$ recombination line emissivity as a function of T_e and $(n_{\rm H^+} \times n_{\rm e})$. For each field, we adopted the value of $E_{\rm em}$ (Pf β) corresponding to its physical conditions. We calculated the values of N_u for the [S III] 18.71 μ m and [S IV] 10.51 μ m considering only collisions with electrons. The values of $E_{\rm em}$ thus calculated are shown in Table 2. Then, using the calculated emissivities and the extinction-corrected line intensities (Table A.3), we estimated $N(S^{++})$, $N(S^{3+})$, and $N(H^{+})$, and their ratios with respect to N(H⁺) in HII, Atomic, DF1, and DF2 using

$$N(S^{+}) = I_{\text{obs}}([SII]) \times 4\pi / E_{\text{em}}([SII])$$
 (2)

$$N(S^{2+}) = I_{\text{obs}}([S \text{ III}]) \times 4\pi/E_{\text{em}}([S \text{ III}])$$
(3)

$$N(S^{3+}) = I_{\text{obs}}([S \text{ IV}]) \times 4\pi/E_{\text{em}}([S \text{ IV}])$$
 (4)

$$N(H^{+}) = I_{\text{obs}}(Pf\beta) \times 4\pi / [E_{\text{em}}(Pf\beta) \times n_e].$$
 (5)

We needed to know $N(S^+)$ in order to account for the total sulfur budget in ionized gas phase. Since there are no near-infrared [S II] lines arising from the ground state, we used the [SII] 6731 Å map from Weilbacher et al. (2015) along with the emissivity calculated with CHIANTI (v10.1.2; Del Zanna et al. 2021) to obtain $N(S^+)$. The $N(S^+)/N(S^{++})$ ratios obtained with our calculations range from 0.15 to 0.18, in agreement with Rubin et al. (2011), who find 0.19 as an upper limit. The elemental abundance of sulfur in the ionized gas is then calculated as $[S/H]_{ionized} = [N(S^{3+}) + N(S^{++}) + N(S^+)]/N(H^+)$. With

Table 2. Abundances of sulfur ions.

ID	Т _е (К)	$n_{\rm e}$ (cm ⁻³)	$E_{\rm em}$ ([SII]) ^(a)	$E_{\rm em}$ ([S III]) ^(b) (erg s ⁻¹)	$E_{\rm em}$ ([S IV]) $^{(c)}$	$E_{\rm em} (Pf\beta)^{(d)}$ (erg cm ⁻³ s ⁻¹)	S+/H+	S++/H+	S ³⁺ /H ⁺	[S/H] _{ion}
H II Atomic DF 1 DF 2	9000 8690 8130 8160	3330 3190 2050 1970	4.85(-17) 4.40(-17) 2.76(-17) 2.70(-17)	3.64(-17) 3.58(-17) 2.73(-17) 2.66(-17)	1.70(-16) 1.65(-16) 1.16(-16) 1.12(-16)	2.42(-27) 2.34(-27) 2.54(-27) 2.54(-27)	1.09(-6) 1.04(-6)	7.08(-6) 6.80(-6)	8.09(-8) 1.63(-7) 2.54(-7) 2.65(-7)	8.33(-6) 8.09(-6)

Notes. (a) Emissivity of the [SII] 6731 Å line per S⁺ atom; (b) emissivity of the [S III] 18 μ m line per S⁺⁺ atom; (c) emissivity of the [S IV] 10 μ m line per S³⁺ atom; (d) emissivity of the Pf β line per $n_{H^+} \times n_e$. Notation: $4.85(-17) = 4.85 \times 10^{-17}$.

these assumptions the S/H ratios are estimated to be 8.40, 8.33, 8.09, and 8.19×10^{-6} , respectively, in the HII, Atomic, DF1, and DF2 regions (see Table 2). These values are roughly consistent with the results of Rubin et al. (2011) who determined S/H = $(7.68\pm0.25)\times10^{-6}$ in the Orion Veil based on near-infrared lines.

The estimated value of S/H toward HII is a factor of $\sim 1.3-1.8$ lower than that derived for the M 42 nebula by previous authors. Esteban et al. (2004) observed a region near the hot star Θ^1 Ori, and measured S/H $\sim 1.65 \times 10^{-5}$ when temperature fluctuations are included and $\sim 1.15 \times 10^{-5}$ when they are not, while McLeod et al. (2016) reported a value of 1.1×10^{-5} toward the Orion Bar. Daflon et al. (2009) estimated the sulfur abundance based on the photospheric lines of a sample of ten B main-sequence stars of the Orion association and obtained S/H = $(1.41\pm0.17) \times 10^{-5}$, which is consistent with the solar value and that of meteorites (Asplund et al. 2006). The estimated S/H ratio in the Orion Veil is, therefore, a factor of ~2 lower than the solar value and that obtained in the M 42 nebula, but still within the uncertainties in this kind of calculation. This discrepancy could originate from the simplicity of our model, which assumes uniform physical conditions along the line of sight, thus neglecting the structure of the ionized gas.

6. Chemical modeling: Atomic sulfur (S)

In this section we model the emission of the H₂ S(1) and [S I] lines in order to determine sulfur depletion in the Orion Bar using the Meudon PDR code³. This code can simulate very detailed micro-physical processes for a given value of the incident UV field and a 1D density structure. As output, it provides the gas and dust temperatures as well as the chemical abundances at each position in the 1D slab, and also performs line and continuum radiative transfer to calculate the integrated emerging fluxes for different inclination angles along the line of sight (Goicoechea & Le Bourlot 2007; Gonzalez Garcia et al. 2008; Le Bourlot et al. 2012; Bron et al. 2014, 2016). Atomic and molecular properties can also be viewed as important parameters of the code. We carefully updated the chemical network, focusing specifically on sulfur species, following the recent studies of Bulut et al. (2021) and Fuente et al. (2019, 2017a) for the CS + O, SO + OH and $O_2 + S$ reactions. In addition, we introduced the experimental photodissociation sections of SH, CS and H₂CS recently implemented by Hrodmarsson & van Dishoeck (2023) as well as the new dissociative recombination rate of SH+ by Boffelli et al. (2023). The final network consists of 3052 gas reactions including photo-reactions. In addition, we added new photo-destruction cross-sections to the Meudon database for SO,

SO₂, CS, O₂, HCN, and HNC, in place of approximate analytical fits, to obtain more accurate predictions. These cross sections were retrieved from the Leiden database⁴, as described in Hrodmarsson & van Dishoeck (2023) and Heays et al. (2017). References to the original sources are given in these papers and in the respective data files. These data were then resampled to fit the needs of the PDR code while keeping the optimal resolution.

Pure gas-phase chemistry is insufficient to explain the abundances of gaseous hydrogen sulfide in the Orion Bar (Goicoechea et al. 2021). A plausible formation channel is provided by surface reactions between accreted atomic sulfur and hydrogen. We included in our chemical network the basic sulfur and oxygen surface chemistry described in Goicoechea et al. (2021) to account for sulfur accretion and hydrogenation on grain surfaces. In particular, we considered the adsorption and desorption of H, H₂, O, O₂, OH, H₂O, CO, S, SH, and H₂S and the formation of H₂, H₂O, and H₂S on the grain surfaces.

Inelastic collisions with electrons, helium, atomic hydrogen and ortho- and para- H_2 need to be taken into account to calculate the excitation of neutral atomic sulfur. We adopted the collision rates with electrons calculated by Tayal (2004). For atomic hydrogen, we used those calculated by Yan & Babb (2023). For helium, we used the collision rates computed by Lique et al. (2018). Motivated by the present study, inelastic collision rates with ortho- and para- H_2 were calculated as explained in the following section.

6.1. Sulfur - H₂ collision rates

The rate coefficients for fine structure excitation of neutral atomic sulfur in collisions with ortho- and para- H_2 for temperatures up to 2000 K were obtained from the corresponding cross sections assuming a Maxwellian velocity distribution. The cross sections utilized were calculated using a quantum-mechanical scattering theory detailed previously by Yan & Babb (2023) with some modifications for the treatment of molecular hydrogen. Potential energy surfaces for the electronic states arising from the interaction of $S(^3P)$ and H_2 were calculated using computational quantum chemical methods with reliable basis sets. The methodology was validated by carrying out additional analogous calculations for the O- H_2 system and good agreement was obtained with previous studies (Flower 1990; Jaquet et al. 1992). A detailed description of the S- H_2 collisional calculations will be presented elsewhere (Yan & Babb, in prep.).

³ https://pdr.obspm.fr

⁴ https://home.strw.leidenuniv.nl/~ewine/photo/index. html

Table 3. Parameters of our reference model.

Parameter	Value	Reference
G_0 at IF	3.1×10^4 Mathis field	Joblin et al. (2018)
G_0 at the back side	3.1×10^3 Mathis field	Joblin et al. (2018)
A_V	20 mag	Joblin et al. (2018)
Inclination angle (i)	60°	Joblin et al. (2018)
Thermal pressure (P_{th})	$2.8 \times 10^{8} \text{ K cm}^{-3}$	Joblin et al. (2018)
$R_V = A_V / E(B - V)$	5.6	Marconi et al. (1998), Witt et al. (2006)
$N_H/E(B-V)$	$1.05 \times 10^{22} \text{ cm}^{-2} \text{ mag}^{-1}$	Joblin et al. (2018)
ζ_{H_2}	$5 \times 10^{-17} \text{ s}^{-1}$	Joblin et al. (2018)
Mass grain/mass gas	0.01	
Grain size distribution	$\propto a^{-3.5}$	Mathis et al. (1997)
Min. grain size	$3 \times 10^{-7} \text{ cm}$	Joblin et al. (2018)
Max. grain size	$3 \times 10^{-5} \text{ cm}$	Joblin et al. (2018)
C/H	1.32×10^{-4}	Savage & Sembach (1996)
O/H	3.19×10^{-4}	Meyer et al. (1998)
S/H	1.86×10^{-5}	Savage & Sembach (1996)
	1.40×10^{-5}	Asplund et al. (2006), Daflon et al. (2009), Goicoechea & Cuadrado (2021)
N/H	7.50×10^{-5}	Meyer et al. (1997)

6.2. Chemical abundances: Reference model

DF3 is the position where the emission of the [S I] 25.249 µm line is highest. This dissociation front is also the most intense in the far-infrared CO lines and in the ground rotational lines of H₂ as shown by Joblin et al. (2018). These authors used the Meudon PDR code to explain the set of observations provided by the Herschel Space Observatory in this PDR. The best fit was obtained assuming a plane-parallel 1D isobaric slab with incident UV field, $G_0 = 3.1 \times 10^4$ Mathis field, thermal pressure, $P_{\rm th} = 2.8 \times 10^8 \ {\rm cm}^{-3} \ {\rm K}$, and cosmic ray ionization rate per ${\rm H}_2$ molecule, $\zeta_{\rm H_2} = 5 \times 10^{-17} \ {\rm s}^{-1}$. The thickness of the slab was assumed to be $A_V=20$ mag and the illumination on the back side ten times lower than that in the side facing the HII region. An inclination angle, i=60° provided the best fit with the observations. The adopted elemental abundances were: $C/H=1.32\times10^{-4}$. O/H=3.19 $\times 10^{-4}$, N/H = 7.50 $\times 10^{-5}$, and S/H=1.86 $\times 10^{-5}$. The value of sulfur abundance is the most uncertain in this list. Recent calculations of the sulfur abundance in the Orion nebula are values closer to S/H=1.40 $\times 10^{-5}$ (Daflon et al. 2009; Goicoechea & Cuadrado 2021), which is consistent with the value in Solar System (Asplund et al. 2006). Taking into account the uncertainties involved in the estimates of the sulfur abundance, we kept S/H=1.86 $\times 10^{-5}$ in our modeling, which is consistent with the upper limit derived by Goicoechea & Cuadrado (2021) in this PDR and provides the best fit to the observations. Hereafter, this set of input parameters is referred to as "reference model" (see Table 3) and will be used to fit the new JWST observations.

Figure 6 shows the gas physical conditions and the fractional abundances of the most abundant carbon and sulfur species as a function of the visual extinction from the IF as predicted by the reference model. We recall that the visual extinction from the IF $(A_V^{\rm IF})$ is different from that along the line of sight $(A_V^{\rm los})$ used in Sect. 4 (see the scheme in Fig. 1). The C⁺ and neutral C carry most of the carbon in gas phase until a visual extinction, $A_V^{\rm IF} \sim 1.3$ mag, where CO becomes the most abundant species. The gas temperature is ~ 200 K and densities are approximately a few times 10^6 cm⁻³ at this visual extinction. Most of the sulfur is in the form of S⁺ and the fractional abundance of S is $\sim 10^{-7}$.

The transition of S⁺/S takes place at a visual extinction, $A_V^{\rm IF}$ ~3 mag, where the gas temperature drops below 100 K and densities are increasing to ~10⁷ cm⁻³. Neutral atomic sulfur remains the main sulfur reservoir until $A_V^{\rm IF}$ ~5 mag. Beyond ~5 mag, most of the sulfur is locked in solid H₂S and the most abundant sulfur species in gas phase are SO, SO₂, and H₂S.

The emission of a given line depends on the abundance of the carrier and local physical conditions. The contribution of each parcel of gas to the observed emission is given by the volume emissivity calculated as $emi = n \times f_u \times E_u \times A_{ij}/(4 \times \pi)$, where n is the gas density and f_u is the fraction of a given species in the upper transition level, and E_u and A_{ij} are the upper level energy and the Einstein spontaneous emission coefficient. In Fig. 6, we show the local emissivities of the H₂ S(1) and [S I] $2\overline{5}.249$ µm lines as a function of A_V^{IF} . While the emissivity of the H₂ S(1) line has a narrow peak at $A_V^{\text{IF}} \sim 1$ mag and drops by several orders of magnitude at $A_V^{IF} > 2$ mag, the emissivity of the [S I] 25.249 µm line has a shallow peak at the same position but remains almost constant, and higher than 10^{-21} erg cm⁻³ s⁻¹ sr⁻¹, until $A_V^{\text{IF}} \sim 5$ mag. This prediction is consistent with the morphology observed in the Orion Bar, where the H₂ S(1) rotational line is mainly tracing the edge-on surface of the PDR, while the [S I] 25.249 µm line arises in the molecular cloud.

We carried out line transfer calculations to predict line intensities and compare with observations on quantitative grounds. The excitation of the [S I] 25.249 μm line is dominated by collisions with ortho- and para-H₂ for $A_V^{\rm IF} > 1$ mag where the gas is mainly in molecular form.

6.3. Predicted line intensities

6.3.1. Reference model

Reference model provides a good guess for the physical parameters in DF3. As commented above, it is the best fitting to the far-infrared CO lines and in the ground rotational lines of H_2 as observed with *Herschel* and reported by Joblin et al. (2018). In Table 4, we compare the intensities of the H_2 S(1) and [S I]

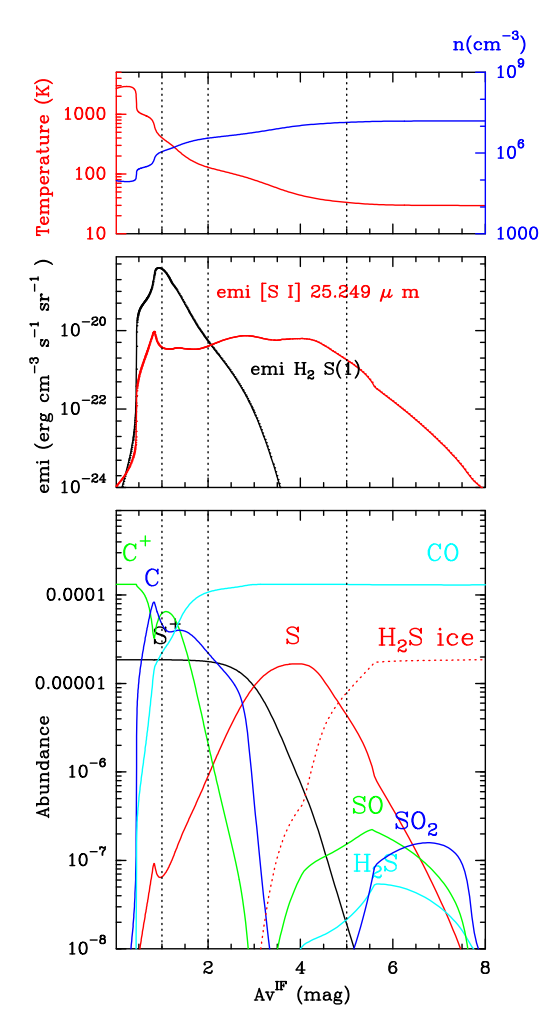


Fig. 6. Predictions of the Meudon PDR code for the reference model. From top to bottom: physical conditions, volume emissivities of the $\rm H_2$ S(1) and [S I] 25.249 μm lines, and chemical abundances relative to hydrogen nuclei as a function of the visual extinction from the HII region ($\rm A_V^{IF}$). The volume emissivity is defined as $emi = n \times f_u \times E_u \times A_{ij}/(4 \times \pi)$, where n is the gas density, f_u is the fraction of particles in the upper level, and E_u and A_{ij} are the upper level energy and the Einstein spontaneous emission coefficient. The transition of S⁺/S takes place at a visual extinction, $A_V^{IF} \sim 3.0$ mag, where the gas temperature drops below 100 K and densities are $\sim 10^7$ cm⁻³. The local volume emissivity of the [S I] 25.249 μm line remains high deeper into the molecular cloud, until $A_V^{IF} \sim 5$ mag. We indicate $A_V^{IF} = 1, 2$, and 5 mag with dashed vertical lines.

25.249 µm lines predicted by reference model with observations. For the computation of these lines we assumed an inclination angle, $i = 60^{\circ}$. Reference model predicts the intensities of the H₂ S(1) and [S I] 25.249 µm lines within a factor of ~3. Moreover, the predicted $I([S I] 25.249 \text{ µm})/I(H_2 \text{ S}(1))$ is a factor of ~3 lower than the observed one, which is a reasonable agreement with observations taking into account the uncertainties in our modeling. It should be noticed that a higher value of i would produce higher line intensities but would not change the $I([S I] 25.249 \text{ µm})/I(H_2 \text{ S}(1))$ ratio. We recall here that our model assumes a S/H = 1.86×10^{-5} , which is consistent with the upper

limit derived by Goicoechea & Cuadrado (2021) on the basis of the sulfur recombination lines. In some sense, this is an upper limit to the possible sulfur elemental abundance. This elemental abundance is in agreement within a factor of 2 with previous results based on ionized and recombination lines (Daflon et al. 2009; Rubin et al. 2011; Goicoechea & Cuadrado 2021). We do not consider that a factor of 2 is significant within the uncertainties of this kind of modeling. Our results support the interpretation that sulfur remains undepleted along the ionized, atomic, and molecular phase in the Orion Bar.

6.3.2. Sensitivity to input parameters

Next we explored the sensitivity of the predicted [S I] 25.249 μ m and H₂ S(1) intensities to different physical parameters. For this purpose, we ran the grid of 1D models described in Table A.4. The computed values of $I([S I] 25.249 \mu m)$, $I(H_2 S(1))$, and $I([S I] 25.249 \mu m)/I(H_2 S(1))$ ratios are listed in Table 4. In models 1 to 5, we investigated the impact of the thermal pressure and the incident UV field on the computed intensities.

The value of $I([S I] 25.249 \mu m)$ increases almost linearly with P_{th} (see models 1 to 3 in Table 4). This is not unexpected because of the high critical density $(n_{\rm H} \sim 10^5 \ {\rm cm}^{-3})$ and upper level energy of this transition (see Table 1). However, I (H₂ S(1)) decreases with increasing P_{th} because higher excited ro-vibrational levels of H₂ become populated. This means that higher values of P_{th} would produce higher values of $I([S I] 25.249 \ \mu m)$ and $I([S I] 25.24 \ \mu m)/I([S I] S(1))$.

Increasing G_0 would lead to higher values of both, $I([S\ I]\ 25.249\ \mu m)$ and $I(H_2\ S(1))$ (see models 2, 4 and 5 in Table 4). One important result is that I ([S\ I]\ 25.249\ \mu m) $<10^{-5}\ {\rm erg\ cm^{-2}\ s^{-1}\ for}\ G_0 < 10^4\ Mathis field.$ This limits the detectability of the [S\ I]\ 25.249\ μm line to the PDRs associated with the HII regions formed by massive stars.

To interpret our observations, it is interesting to explore the influence of other parameters such as $\zeta_{\rm H_2}$, $N_{\rm H}/E(B-V)$ ratio, and S/H. The comparison of models 2 and 6 shows that increasing the value of $\zeta_{\rm H_2}$ by a factor of 10 produces minor changes in the intensities of both lines. Therefore, we do not expect that possible uncertainties in the value of $\zeta_{\rm H_2}$ would affect our conclusions.

The dust extinction curve is not well known, and several values of $N_{\rm H}/E(B-V)$ have been used in the literature (Cardelli et al. 1989; Joblin et al. 2018; Habart et al. 2024). In particular, Habart et al. (2024) used $N_{\rm H}/E(B-V)=1.6\times 10^{22}~{\rm cm}^{-2}~{\rm mag}^{-1}$ from Cardelli et al. (1989). In order to test the impact of this parameter we ran model 7. Changing $N_{\rm H}/E(B-V)$ ratio (models 2 and 7) have a significant impact on I ([S I] 25.249 μ m) and I (H₂ S(1)) but the I([S I] 25.249 μ m)/I(H₂ S(1)) ratio is little affected.

As expected, varying S/H has a large impact of the intensity of the [S I] 25.249 μ m line, which scales almost linearly with S/H, but has no significant impact of the intensity of the H₂ S(1) line (models 2 and 8). Therefore, the $I([S I] 25.249 \mu m)/I(H_2 S(1))$ ratio increases with S/H and can be used as a tracer of S/H in PDRs as long as P_{th} and G_0 are known. Therefore, the study of neutral atomic sulfur in PDRs through the observation of the [S I] 25.249 μ m fine-structure line can provide a good estimate of sulfur depletion in this kind of region.

6.4. Limitations of our modeling

In this section, we revise the uncertainties in the sulfur chemistry that could affect our results. The uncertainties in the adsorption

Table 4. Comparison between predicted (for $i = 60^{\circ}$) and observed intensities (erg cm⁻² s⁻¹ sr⁻¹).

$I[H_2 S(1)]$	<i>I</i> ([S I] 25.249 μm)	<u>I([SI] 25.249 μm)</u> <u>I[H₂ S(1)]</u>	Models
1.16(-3)(*)	3.72(-6)	0.003	Model 1 ($P = 2.8 \times 10^7 \text{ K cm}^{-3}$)
7.61(-4)	2.80(-5)	0.04	Model 2 ($P = 2.8 \times 10^8 \text{ K cm}^{-3}$)
4.86(-4)	4.58(-4)	0.94	Model 3 ($P = 2.8 \times 10^9 \text{ K cm}^{-3}$)
1.98(-4)	1.37(-5)	0.07	Model 4 ($G_0 = 3.1 \times 10^3$ Mathis field)
1.12(-3)	2.44(-4)	0.21	Model 5 ($G_0 = 3.1 \times 10^5$ Mathis field)
7.57(-4)	2.69(-5)	0.03	Model 6 ($\zeta_{H_2} = 5 \times 10^{-16} \text{ s}^{-1}$)
1.11(-3)	4.65(-5)	0.04	Model 8 $(N_H/E(B-V) = 1.6 \times 10^{22} \text{ cm}^{-2} \text{ mag}^{-1})$
7.23(-4)	2.00(-7)	0.0004	Reference (S/H = 1.86×10^{-7})
8.95(-4)	4.23(-5)	0.05	Reference (S/H = 1.86×10^{-5})
8.62(-4)	1.19(-4)	0.14	DF3

Notes. In this table, only the model parameters relevant for the discussion in Sect. 6.3 are shown. The complete set of input parameters are given in Table 3 and Table A.4. (*) $1.16(-3) = 1.16 \times 10^{-3}$.

and desorption processes of sulfur species, in particular atomic sulfur, on the grain surfaces could have a significant impact on the predicted chemical abundances. Indeed, the binding energies of the sulfur species on the grain surfaces are not fully understood yet. Perrero et al. (2022) calculated the binding energies of S, SH, and H₂S in amorphous and crystalline ice. They found that each species experience different binding energies depending on its position in the ice structure. In general, binding energies are higher in crystalline than in amorphous water ice. In amorphous ice, they found a range of values for the binding energy of a given species with variations of up to a factor of 2 depending on the adsorption site. Binding energies previously reported by Wakelam et al. (2017) and Das et al. (2018) are placed within this range. Perrero et al. (2024) estimated the binding energies of sulfur species on bare silicate grains. Their results show that binding energies in bare grains are a factor of 2-4 higher than those in amorphous ice. In our model, we adopted BE (H_2S) = BE (SH) = 2700 K, which are at the lower end of the range values published by Perrero et al. (2022) in amorphous ice, and the ones reported by Wakelam et al. (2017). For atomic sulfur, we adopted BE(S)=1800 K, close to the minimum value reported by Perrero et al. (2022) in amorphous ice and consistent with the experiments by Jiménez-Escobar & Muñoz Caro (2011). These values were also used by Cazaux et al. (2022) to investigate the formation of allotropes on grain surfaces. Therefore, the adopted binding energies lie at the lower end of the possible values, hence maximizing the amount of sulfur in gas phase.

Nonthermal processes can also contribute to release sulfur species to the gas phase in PDRs. Unfortunately, only the $\rm H_2S$ photo-desorption yield in pure $\rm H_2S$ ice has been estimated thus far. Based on laboratory experiments, Fuente et al. (2017b) determined the photo-desorption yield of $\rm H_2S$ to be 1.2×10^{-3} per molecule and incident photon. For the other sulfur species, we assumed 1×10^{-4} per particle and photon following Hasegawa & Herbst (1993). Laboratory experiments to measure the photo-desorption yields for all sulfur species would be desirable in order to have a more accurate description of the gas-dust interaction.

To test the influence of the adopted binding energies and photo-desorption yields on the predicted intensity of the [S I] 25.249 μ m line, we ran a pure gas-phase model (i.e., neglecting adsorption and desorption on grain surfaces) using the input parameters in Table 3. As expected, the $I([S I] 25.249 \mu m)$ and

 $I([S\ I]\ 25.249\ \mu m)/I(H_2\ S(1))$ ratios increase but the model falls short, by a factor of ~2, in the prediction of the observed intensity.

The discrepancy between model and observations can also be due to the assumed physical structure. As commented above, the intensity of the [S I] 25.249 µm line is very sensitive to assumed thermal pressure. High angular resolution images (~1") of the CO $J = 3 \rightarrow 2$ line revealed the presence of fragmentation and photo-evaporation flows in the Orion Bar (Goicoechea et al. 2016). Bron et al. (2018) developed a 1D hydrodynamical PDR code coupling hydrodynamics, extreme-ultraviolet and FUV radiative transfer, and time-dependent thermochemical evolution to simulate an UV-illuminated molecular cloud that is evaporating into a surrounding low-pressure medium. They found that, although moderate pressure gradients can develop in this scenario, isobaric PDR models are a better approximation to the structure of photoevaporating PDRs than constant-density PDR models. The reference model is therefore our best approximation to the physics and chemistry in the Orion Bar. Though small departures in the physical structure from the isobaric case, for example variations in the density, are not unreasonable and could help reconcile model predictions and observations.

7. Discussion

We used high sensitivity JWST observations to estimate the sulfur abundance in the ionized and warm molecular layer of the Orion Bar. The detection of the [S I] 25.249 μ m line shows that sulfur is undepleted in the warm molecular gas.

The lack of sulfur depletion in the warm molecular gas of the Orion Bar challenges our understanding of sulfur chemistry. In order to explain the high value of sulfur depletion estimated in dark clouds (see, e.g., Fuente et al. 2019), it has been proposed that most of the sulfur can be locked in (semi-)refractories such as iron sulfide and sulfur allotropes in these cold clouds (Jiménez-Escobar & Muñoz Caro 2011; Jiménez-Escobar et al. 2012; Fuente et al. 2019; Kama et al. 2019; Shingledecker et al. 2020; Cazaux et al. 2022). Refractory material presents sub-limation temperatures higher than a few hundred K and can only be evaporated in extremely hot regions ($T \sim 1000 \text{ K}$) such as the innermost regions of protoplanetary disks (Kama et al. 2019). This is the case of FeS with a sublimation temperature of $\sim 655 \text{ K}$ (Lodders 2003) and the S_n chains with n > 2, which have sublimation temperatures of more than a few hundred kelvin

(Jiménez-Escobar & Muñoz Caro 2011; Cazaux et al. 2022). In the ionized gas of the M 42 nebula, dust temperatures are high enough to sublimate this (semi-)refractory material and one would expect that sulfur is essentially undepleted. However, this is not the case for the molecular gas in the Orion Bar. The grains located at $A_{\rm V}^{\rm IF}$ > 3 mag in DF3 have temperatures of ~40–100 K, clearly insufficient to destroy refractories. One could argue that the physical conditions in the Orion Bar are not adequate to form these compounds. Cazaux et al. (2022) proposed that sulfur allotropes form in the diffuse envelopes of molecular clouds. Based on the treatment developed by Umebayashi & Nakano (1980) and Draine & Sutin (1987) for collisions with charged grains, Ruffle et al. (1999) proposed that the sticking coefficient of positive ions such as S⁺ increases in regions where the grains are negatively charged, hence enhancing the relative abundance of S respect to H on grain surfaces and promoting the formation of sulfur chains. This mechanism works in diffuse clouds but can be inefficient for the conditions of the Orion Bar where grain charges are more positive and dust temperatures are higher.

However, the above stationary description may not be realistic enough to simulate the expansion of an HII region into the parent molecular cloud. In OMC 1, for instance, the UV radiation from the Trapezium cluster is eroding the molecular cloud from which the stars were formed. Since sulfur refractories would survive under the physical conditions prevailing in the PDR, the lack of sulfur depletion in the Orion Bar could be the consequence of the absence of these compounds in the initial molecular cloud. Within the European Millimeter Radio Astronomy Institute (IRAM) Large Program "Gas-phase Elemental abundances in Molecular cloudS" (GEMS; PI: Asunción Fuente), Fuente et al. (2023) determined the sulfur elemental abundance in three cuts in Orion A. These cuts were selected in OMC-2, OMC-3, and OMC-4, at distances >1 pc from M 42. These cuts were selected in quiescent regions, avoiding the location of protostars and energetic outflows that could destroy interstellar grains. Nevertheless, they obtained that their observations were better explained assuming undepleted sulfur. This behavior is different from that observed by the same authors in the low-mass star-forming regions Taurus and Perseus, where sulfur was estimated to be depleted by a factor of >10.

Although some sulfur species such as CS and SO are routinely observed in the interstellar medium, there are very few estimates of sulfur depletion in other PDRs. Goicoechea et al. (2006) determined that sulfur depletion is $\sim 4-5$ in the PDR associated with the Horsehead nebula on the basis of CS and HCS+ millimeter observations. The Horsehead nebula is the only region where a gas-phase doubly sulfuretted species, S2H, has been detected (Fuente et al. 2017b). The detection of this species is suggestive of the presence of larger sulfur chains. This PDR is illuminated by a low UV field, $G_0 = 60$, and presents a differentiated chemistry from the Orion Bar. One main difference is that the dust temperature is around ~20-30 K, which is below the sublimation temperature of most species, including atomic sulfur (~58 K, Wakelam et al. 2017). This would allow the development of a rich chemistry on the irradiated grain surfaces and most likely, the formation of progressively larger sulfur chains. Rivière-Marichalar et al. (2019) carried out a complete inventory of sulfur species using the "Horsehead Wide-band High-resolution Iram-30 m Surveys at two positions with Emir Receivers" (WHISPER; PI: Jerome Pety, Guzmán et al. 2012) data and found the abundances of sulfur species in the cold core close to the Horsehead nebula is similar to those found in dark clouds like TMC 1 (CP).

Still, there are many open questions to understand sulfur chemistry in the interstellar medium. The formation and destruction mechanisms of sulfur allotropes are poorly known. In particular, there is no information on the behavior of long sulfur chains under UV irradiation. One could think that large allotropes such as S₃ and/or S₈ could be photo-dissociated on the grain surfaces, breaking into smaller chains that sublimate at lower dust temperatures. In this case, large sulfur chains could be destroyed in UV-irradiated environments although dust temperatures were below their sublimation temperatures. If, alternatively, one thinks that the amount of sulfur in volatiles and refractories is preserved in the molecular gas during the expansion of the HII region, sulfur depletion would be determined by the initial composition of the molecular cloud. The observation of sulfur species in PDRs with different physical conditions and their host molecular clouds would be useful to discern between these two scenarios. In this context, the study of neutral atomic sulfur in PDRs through the observation of the [S I] 25.249 µm fine-structure line using the JWST is a valuable tool for determining the amount of sulfur in volatiles and the mechanisms that subtract sulfur atoms from the gas phase in the interstellar medium.

8. Summary and conclusions

The JWST (Gardner et al. 2006) ERS program "PDRs4All: Radiative feedback from massive stars" has observed the prototypical PDR usually referred to as the Orion Bar as a template for the study of Galactic and extragalactic PDRs (Berné et al. 2022). We used the PDRs4All data to estimate the amount of sulfur in the Orion Bar. Our results can be summarized as follows:

- The high sensitivity of JWST has provided the first detection of the [S I] $25.249 \mu m$ line in the Orion Bar. This is also the first detection in a PDR;
- We have estimated a sulfur abundance of S/H $\sim 8 \times 10^{-6}$ in the ionized gas. This implies a sulfur depletion lower than a factor of 2 in the Orion Veil;
- Our team has upgraded the Meudon PDR code chemical network to account for the observations of neutral atomic sulphur:
- Chemical modeling of DF3 shows that, as expected, most of the sulfur is in the form of S⁺ in the outer layers of the PDR. The S⁺/S transition takes place at a visual extinction, $A_V^{\rm IF} \sim 3$ mag. For $A_V^{\rm IF} > 3$ mag, neutral atomic sulfur remains the main sulfur reservoir until $A_V^{\rm IF} \sim 5$ mag. Beyond ~ 5 mag, most of the sulfur is locked in solid H₂S and the most abundant sulfur species in the gas phase are SO, SO₂, and H₂S:
- New inelastic collision rates of atomic sulfur (S) with H, H_2 , and He were used to carry out excitation and radiative transfer calculations to compute the [S I] 25.249 μ m line intensities. Our predictions show that the emission of the [S I] 25.249 μ m line arises in molecular gas located at a visual extinction of ~1–5 mag from the dissociation front. In this region, the excitation of the line is mainly through collisions with H_2 ;
- A detailed comparison of our modeling with observations shows that sulfur is undepleted in the warm molecular gas associated with the Orion Bar.

The JWST data have allowed us to probe the ionized and molecular gas associated with the Orion Bar. Our results show that all the observations can be explained with a moderate sulfur depletion, lower than a factor of ~2, along this PDR. This is consistent with recent results that suggest that sulfur depletion is lower in massive star-forming regions than in dark clouds because of the higher incident UV field (Fuente et al. 2023). Several scenarios are discussed to account for the lack of sulfur depletion in the Orion molecular cloud.

Acknowledgements. This work is based on observations made with the NASA/ESA/CSA James Webb Space Telescope. The data were obtained from the Mikulski Archive for Space Telescopes at the Space Telescope Science Institute, which is operated by the Association of Universities for Research in Astronomy, Inc., under NASA contract NAS 5-03127 for JWST. These observations are associated with program #1288. Support for program #1288 was provided by NASA through a grant from the Space Telescope Science Institute, which is operated by the Association of Universities for Research in Astronomy, Inc., under NASA contract NAS 5-03127. AF thanks the Spanish MICIN for funding support from PID2019-106235GB-I00 and the European Research Council (ERC) for funding under the Advanced Grant project SUL4LIFE, grant agreement no. 101096293. AF also thanks project PID2022-137980NB-I00 funded by the Spanish Ministry of Science and Innovation/State Agency of Research MCIN/AEI/ 10.13039/501100011033 and by "ERDF A way of making Europe". E.P. acknowledges support from the University of Western Ontario, the Institute for Earth and Space Exploration, the Canadian Space Agency (CSA, 22JWGO1-16), and the Natural Sciences and Engineering Research Council of Canada. TO is supported by JSPS Bilateral Program, Grant Number 120219939. J.F.B. and P.G.Y. are supported in part by NASA APRA grant 80NSSC19K0698. M.G.W. was supported in part by NASA grant JWST-AR-01557.001-A. Work by Y.O. and M.R. is carried out within the Collaborative Research Centre 956, sub-project C1, funded by the Deutsche Forschungsgemeinschaft (DFG) – project ID 184018867. J.R.G. thanks the Spanish MCIN for funding support under grant PID2019-106110GB-I00.

A114

```
References
Abel, N. P., Brogan, C. L., Ferland, G. J., et al. 2004, ApJ, 609, 247
Abel, N. P., Ferland, G. J., O'Dell, C. R., Shaw, G., & Troland, T. H. 2006, ApJ,
  644, 344
Anderson, D. E., Bergin, E. A., Maret, S., & Wakelam, V. 2013, ApJ, 779, 141
Argyriou, I., Glasse, A., Law, D. R., et al. 2023, A&A, 675, A111
Asplund, M., Grevesse, N., & Jacques Sauval, A. 2006, Nucl. Phys. A, 777, 1
Bally, J., O'Dell, C. R., & McCaughrean, M. J. 2000, AJ, 119, 2919
Berné, O., Habart, É., Peeters, E., et al. 2022, PASP, 134, 054301
Berné, O., Martin-Drumel, M.-A., Schroetter, I., et al. 2023, Nature, 621, 56
Berné, O., Habart, E., Peeters, E., et al. 2024, Science, 383, 988
Bockelée-Morvan, D. & Biver, N. 2017, Philos. Trans. Roy. Soc. Lond. Ser. A,
      , 20160252
Boffelli, J., Gauchet, F., Kashinski, D. O., et al. 2023, MNRAS, 522, 2259
Booth, A. S., Walsh, C., Terwisscha van Scheltinga, J., et al. 2021, Nat. Astron.,
  5, 684
Bregman, J., Larson, K., Rank, D., & Temi, P. 1994, ApJ, 423, 326
Bron, E., Le Bourlot, J., & Le Petit, F. 2014, A&A, 569, A100
Bron, E., Le Petit, F., & Le Bourlot, J. 2016, A&A, 588, A27
Bron, E., Agúndez, M., Goicoechea, J. R., & Cernicharo, J. 2018, arXiv e-prints
  [arXiv:1801.01547]
Bulut, N., Roncero, O., Aguado, A., et al. 2021, A&A, 646, A5
Burton, M. G., Hollenbach, D. J., & Tielens, A. G. G. M. 1990, ApJ, 365, 620
Capria, M. T., Capaccioni, F., Filacchione, G., et al. 2017, MNRAS, 469, S685
Cardelli, J. A., Clayton, G. C., & Mathis, J. S. 1989, ApJ, 345, 245
Caselli, P. 2020, Phys. Life Rev., 32, 117
Cazaux, S., Carrascosa, H., Muñoz Caro, G. M., et al. 2022, A&A, 657, A100
Chown, R., Sidhu, A., Peeters, E., et al. 2024, A&A, 685, A75 (Paper IV)
Daflon, S., Cunha, K., de la Reza, R., Holtzman, J., & Chiappini, C. 2009, AJ,
Das, A., Sil, M., Gorai, P., Chakrabarti, S. K., & Loison, J. C. 2018, ApJS, 237, 9
Del Zanna, G., Dere, K. P., Young, P. R., & Landi, E. 2021, ApJ, 909, 38
Draine, B. T., & Sutin, B. 1987, ApJ, 320, 803
Ehrenfreund, P., Elsaesser, A., & Groen, J. 2015, Highlights Astron., 16, 709
Esteban, C., Peimbert, M., García-Rojas, J., et al. 2004, MNRAS, 355, 229
Flower, D. R. 1990, MNRAS, 242, 1P
Fuente, A., Rodriguez-Franco, A., & Martin-Pintado, J. 1996, A&A, 312, 599
Fuente, A., Rodriguez, A., Garcia-Burillo, S., Martin-Pintado, J., & Black, J. H.
   2003, A&A, 406, 899
Fuente, A., Gerin, M., Pety, J., et al. 2017a, A&A, 606, L3
Fuente, A., Goicoechea, J. R., Pety, J., et al. 2017b, ApJ, 851, L49
Fuente, A., Navarro, D. G., Caselli, P., et al. 2019, A&A, 624, A105
Fuente, A., Rivière-Marichalar, P., Beitia-Antero, L., et al. 2023, A&A, 670,
```

```
Gardner, J. P., Mather, J. C., Clampin, M., et al. 2006, Space Sci. Rev., 123, 485
Goicoechea, J. R., & Cuadrado, S. 2021, A&A, 647, A7
Goicoechea, J. R., & Le Bourlot, J. 2007, A&A, 467, 1
Goicoechea, J. R., Pety, J., Gerin, M., et al. 2006, A&A, 456, 565
Goicoechea, J. R., Joblin, C., Contursi, A., et al. 2011, A&A, 530, L16
Goicoechea, J. R., Pety, J., Cuadrado, S., et al. 2016, Nature, 537, 207
Goicoechea, J. R., Aguado, A., Cuadrado, S., et al. 2021, A&A, 647, A10
Gonzalez Garcia, M., Le Bourlot, J., Le Petit, F., & Roueff, E. 2008, A&A, 485,
Gordon, K. D., Bohlin, R., Sloan, G. C., et al. 2022, AJ, 163, 267
Guzmán, V., Pety, J., Gratier, P., et al. 2012, A&A, 543, A1
Guzmán, V. V., Öberg, K. I., Huang, J., Loomis, R., & Qi, C. 2017, ApJ, 836, 30
Haas, M. R., Hollenbach, D. J., & Erickson, E. F. 1986, ApJ, 301, L57
Habart, E., Peeters, E., Berné, O., et al. 2024, A&A, 685, A73 (Paper II)
Hasegawa, T. I., & Herbst, E. 1993, MNRAS, 261, 83
Hayashi, M., Hasegawa, T., Gatley, I., Garden, R., & Kaifu, N. 1985, MNRAS,
Heays, A. N., Bosman, A. D., & van Dishoeck, E. F. 2017, A&A, 602, A105
Hily-Blant, P., Pineau des Forêts, G., Faure, A., & Lique, F. 2022, A&A, 658,
Hogerheijde, M. R., Jansen, D. J., & van Dishoeck, E. F. 1995, A&A, 294, 792
Hrodmarsson, H. R., & van Dishoeck, E. F. 2023, A&A, 675, A25
Jaquet, R., Staemmler, V., Smith, M. D., & Flower, D. R. 1992, J. Phys. B At.
   Molec. Phys., 25, 285
Jensen, S. S., Jørgensen, J. K., Kristensen, L. E., et al. 2019, A&A, 631, A25
Jiménez-Escobar, A. & Muñoz Caro, G. M. 2011, A&A, 536, A91
Jiménez-Escobar, A., Muñoz Caro, G. M., Ciaravella, A., et al. 2012, ApJ, 751,
Joblin, C., Bron, E., Pinto, C., et al. 2018, A&A, 615, A129
Kama, M., Shorttle, O., Jermyn, A. S., et al. 2019, ApJ, 885, 114
Kramida, A., Yu. Ralchenko, Reader, J., & NIST ASD Team 2022, NIST Atomic
   Spectra Database (ver. 5.10), https://physics.nist.gov/asd. (National
   Institute of Standards and Technology, Gaithersburg, MD, USA)
Le Bourlot, J., Le Petit, F., Pinto, C., Roueff, E., & Roy, F. 2012, A&A, 541, A76
Lique, F., Kłos, J., & Le Picard, S. D. 2018, Phys. Chem. Chem. Phys. (Incorp.
   Faraday Trans.), 20, 5427
Lodders, K. 2003, ApJ, 591, 1220
Marconi, A., Testi, L., Natta, A., & Walmsley, C. M. 1998, A&A, 330, 696
Mathis, J. S., Rumpl, W., & Nordsieck, K. H. 1977, ApJ, 217, 425
Meyer, D. M., Cardelli, J. A., & Sofia, U. J. 1997, ApJ, 490, L103
Meyer, D. M., Jura, M., & Cardelli, J. A. 1998, ApJ, 493, 222
McLeod, A. F., Weilbacher, P. M., Ginsburg, A., et al. 2016, MNRAS, 455, 4057
Menten, K. M., Reid, M. J., Forbrich, J., & Brunthaler, A. 2007, A&A, 474, 515
Neufeld, D. A., Godard, B., Gerin, M., et al. 2015, A&A, 577, A49
Omodaka, T., Hayashi, M., Hasegawa, T., & Hayashi, S. S. 1994, ApJ, 430, 256
Ossenkopf, V., & Henning, T. 1994, A&A, 291, 943
Patapis, P., Argyriou, I., Law, D. R., et al. 2024, A&A, 682, A53
Peeters, E., Habart, E., Berné, O., et al. 2024, A&A, 685, A74 (Paper III)
Peimbert, M., & Torres-Peimbert, S. 1977, MNRAS, 179, 217
Perrero, J., Enrique-Romero, J., Ferrero, S., et al. 2022, ApJ, 938, 158
Perrero, J., Beitia-Antero, L., Fuente, A., Ugliengo, P., & Rimola, A. 2024,
   MNRAS, 527, 10697
Rivière-Marichalar, P., Fuente, A., Goicoechea, J. R., et al. 2019, A&A, 628, A16
Roueff, E., Abgrall, H., Czachorowski, P., et al. 2019, A&A, 630, A58
Rubin, R. H., Simpson, J. P., O'Dell, C. R., et al. 2011, MNRAS, 410, 1320
Ruffle, D. P., Hartquist, T. W., Caselli, P., & Williams, D. A. 1999, MNRAS, 306,
Savage, B. D., & Sembach, K. R. 1996, ARA&A, 34, 279
Shingledecker, C. N., Lamberts, T., Laas, J. C., et al. 2020, ApJ, 888, 52
Sofia, U. J., Cardelli, J. A., & Savage, B. D. 1994, ApJ, 430, 650
Storey, P. J., & Hummer, D. G. 1995, MNRAS, 272, 41
Tauber, J. A., Tielens, A. G. G. M., Meixner, M., & Goldsmith, P. F. 1994, ApJ,
   422, 136
Tauber, J. A., Lis, D. C., Keene, J., Schilke, P., & Buettgenbach, T. H. 1995,
   A&A, 297, 567
Tayal, S. S. 2004, ApJS, 153, 581
Umebayashi, T., & Nakano, T. 1980, PASJ, 32, 405
Van De Putte, D., Meshaka, R., Trahin, B., et al. 2024, A&A, 687, A86
   (Paper VIII)
Vastel, C., Quénard, D., Le Gal, R., et al. 2018, MNRAS, 478, 5514
Vidal, T. H. G., Loison, J.-C., Jaziri, A. Y., et al. 2017, MNRAS, 469, 435
Wakelam, V., Loison, J. C., Mereau, R., & Ruaud, M. 2017, Mol. Astrophys., 6,
Wang, K. S., Bourke, T. L., Hogerheijde, M. R., et al. 2013, A&A, 558, A69
Weilbacher, P. M., Monreal-Ibero, A., Kollatschny, W., et al. 2015, A&A, 582,
Wells, M., Pel, J. W., Glasse, A., et al. 2015, PASP, 127, 646
White, G. J., & Sandell, G. 1995, A&A, 299, 179
```

Witt, A. N., Gordon, K. D., Vijh, U. P., et al. 2006, ApJ, 636, 303 Yan, P.-G., & Babb, J. F. 2023, MNRAS, 522, 1265 Zannese, M., Tabone, B., Habart, E., et al. 2024, Nat. Astron., 8, 577

- ¹ Centro de Astrobiología (CAB), CSIC-INTA, Ctra. de Torrejón a Ajalvir, km 4, 28850 Torrejón de Ardoz, Spain e-mail: afuente@cab.inta-csic.es
- ² LERMA, Observatoire de Paris, PSL Research University, CNRS, Sorbonne Universités, 92190 Meudon, France
- ³ Astronomy Department, University of Maryland, College Park, MD 20742, USA
- ⁴ Center for Astrophysics | Harvard & Smithsonian, MS 14, 60 Garden St., Cambridge, MA 02138, USA
- Department of Astronomy, Graduate School of Science, The University of Tokyo, 7-3-1 Hongo, Bunkyo-ku, Tokyo 113-0033, Japan
- ⁶ Department of Space, Earth and Environment, Chalmers University of Technology, Onsala Space Observatory, 439 92 Onsala, Sweden
- Institut de Recherche en Astrophysique et Planétologie, Université Toulouse III – Paul Sabatier, CNRS, CNES, 9 Av. du colonel Roche, 31028 Toulouse Cedex 04, France
- ⁸ Space Telescope Science Institute, 3700 San Martin Drive, Baltimore, MD 21218, USA
- Department of Physics & Astronomy, The University of Western Ontario, London ON N6A 3K7, Canada
- ¹⁰ Institute for Earth and Space Exploration, The University of Western Ontario, London ON N6A 3K7, Canada
- ¹¹ Institut d'Astrophysique Spatiale, Université Paris-Saclay, CNRS, Bâtiment 121, 91405 Orsay Cedex, France

- ¹² Department of Astronomy, University of Michigan, 1085 South University Avenue, Ann Arbor, MI 48109, USA
- ¹³ Carl Sagan Center, SETI Institute, 339 Bernardo Avenue, Suite 200, Mountain View, CA 94043, USA
- ¹⁴ Instituto de Física Fundamental (CSIC), Calle Serrano 121–123, 28006 Madrid, Spain
- ¹⁵ I. Physikalisches Institut der Universität zu Köln, Zülpicher Straße 77, 50937 Köln, Germany
- ¹⁶ Physikalischer Verein Gesellschaft für Bildung und Wissenschaft, Robert-Mayer-Str. 2, 60325 Frankfurt, Germany
- 17 Goethe-Universität, Physikalisches Institut, Frankfurt am Main, Germany
- ¹⁸ Institut de Planétologie et d'Astrophysique de Grenoble (IPAG), Université Grenoble Alpes, CNRS, 38000 Grenoble, France
- ¹⁹ Institut de Radioastronomie Millimétrique (IRAM), 300 Rue de la Piscine, 38406 Saint-Martin-d'Hères, France
- ²⁰ Instituto de Matemática, Estatística e Física, Universidade Federal do Rio Grande, 96201-900 Rio Grande, RS, Brazil
- ²¹ INAF Osservatorio Astrofisico di Catania, Via Santa Sofia 78, 95123 Catania, Italy
- ²² AIM, CEA, CNRS, Université Paris-Saclay, Université Paris Diderot, Sorbonne Paris Cité, 91191 Gif-sur-Yvette, France
- ²³ Department of Physics, College of Science, United Arab Emirates University (UAEU), Al-Ain 15551, UAE
- ²⁴ Star and Planet Formation Laboratory, RIKEN Cluster for Pioneering Research, Wako, Saitama 351-0198, Japan
- ²⁵ Department of Physics and Astronomy, University of Georgia, Athens, GA 30602-2451, USA
- ²⁶ Université Paris Cité, 85 Bd. Saint-Germain, 75006 Paris, France

Appendix A: Complementary tables and figure

Table A.1. Field descriptions (the nomenclature and A_V values are taken from Peeters et al. 2024).

ID	RA(J2000)	Dec(J2000)	Size	PA	$A_{\rm V}({\rm bar})^1$	$A_{\rm V}({\rm bar})^2$	$A_{\rm V}({\rm foreground})^3$
H II region	05:35:20.187	-05:24:59.81	1.5"×6"	40	0	0	1.5
Atomic	05:35:20.259	-05:25:02.52	3"×6"	40	4.33	7.86	1.3
DF 1	05:35:20.512	-05:25:11.95	3"×6"	40	9.34	37.34	1.2
DF 2	05:35:20.615	-05:25:14.71	4"×6"	40	4.67	8.67	1.2
DF 3	05:35:20.745	-05:25:20.56	4"×6"	40	2.00	3.22	1.4

¹Internal PDR extinction calculated using the foreground formalism; ²Internal PDR extinction calculated using the intermingled formalism; ³ Foreground extinction. Nomenclature and $A_{\rm V}$ values are taken from Peeters et al. (2024).

Table A.2. Uncorrected line fluxes (erg cm⁻² s⁻¹ sr⁻¹).

ID	$H_2 (17.035 \mu m)^a$	SI (25.24 μm)	SIII (18.7 μm) ^a	SIV (10.5 μm) ^a
	$\times 10^{-4}$	$\times 10^{-5}$	$\times 10^{-2}$	$\times 10^{-3}$
HII region	2.00	< 1.2 ^b	6.02	3.10
Atomic	1.63	$< 2.4^{b}$	4.07	4.18
DF1	2.45	$< 2.3^{b}$	1.80	2.75
DF2	7.17	5.7 (0.9)	1.58	2.50
DF3	7.81	11.4 (0.7)	1.27	1.94

 $[^]a$ The error is dominated by the calibration uncertainty (10%). b 3×rms upper limits.

Table A.3. Extinction-corrected fluxes (erg cm $^{-2}$ s $^{-1}$ sr $^{-1}$).

ID	H ₂ (17.035 μm) ^a	[S I] (25.249 μm) ^a	[S III] (18.7 μm) ^b	[S IV] (10.5 μm) ^b
	$\times 10^{-4}$	$\times 10^{-5}$	$\times 10^{-2}$	$\times 10^{-3}$
HII region	2.09	< 1.2	6.29	3.39
Atomic	1.92 - 2.12	< 2.8	4.23	4.51
DF1	3.33 - 7.50	< 3.7	1.86	2.95
DF2	8.50-9.55	6.14-6.46	1.64	2.68
DF3	8.62-8.93	11.90-12.09	1.32	2.11

^a Lower and upper limits to the extinction-corrected fluxes obtained using $[A_V \text{ (foreground)} + A_V \text{ (bar)}^1]$ and $[A_V \text{ (foreground)} + A_V \text{ (bar)}^2]$, respectively. For the upper limits we only used $A_V \text{ (foreground)} + A_V \text{ (bar)}^2$.

^b Extinction-corrected fluxes obtained using $A_V \text{ (foreground)}$.

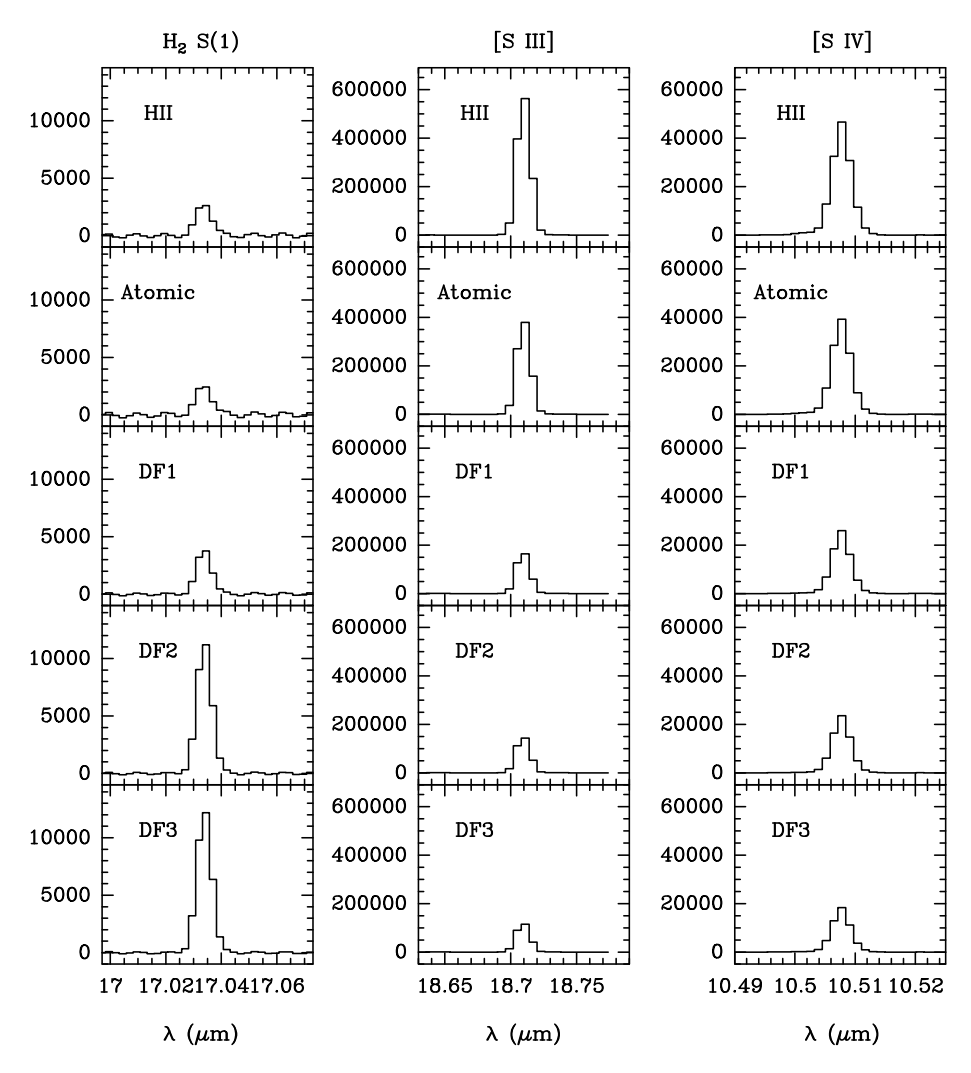


Fig. A.1. Average intensity spectra of the H_2 S(1), [S III] 18.713 μm , and [S IV] 10.5105 μm lines in the fields shown in Fig. 5. The intensity scale is MJy sr⁻¹.

Table A.4. Input parameters for chemical models.¹

Model	Parameter	Value
1	G_0 at IF	3.1×10^4
	G_0 at the back side	0.1
	Inclination angle (i)	60°
	Thermal pressure (P_{th})	$2.8 \times 10^7 \text{ K cm}^{-3}$
	$N_H/E(B-V)$	$1.05 \times 10^{22} \text{ cm}^2 \text{ mag}^{-1}$
		$5 \times 10^{-17} \text{ s}^{-1}$
	ζ_{H_2}	
	S/H	1.86×10^{-5}
2	G_0 at IF	3.1×10^4
	G_0 at the back side	0.1
	Inclination angle (i)	60°
	Thermal pressure (P_{th})	$2.8 \times 10^8 \text{ K cm}^{-3}$
	$N_H/E(B-V)$	$1.05 \times 10^{22} \text{ cm}^2 \text{ mag}^{-1}$
	ζ_{H_2}	$5 \times 10^{-17} \text{ s}^{-1}$
	S/H	1.86×10^{-5}
3	G ₀ at IF	3.1×10^4
	G_0 at the back side.	0.1
	Inclination angle (i)	60°
	Thermal pressure (P_{th})	$2.8 \times 10^9 \text{ K cm}^{-3}$
	$N_H/E(B-V)$	$1.05 \times 10^{22} \text{ cm}^2 \text{ mag}^{-1}$ $5 \times 10^{-17} \text{ s}^{-1}$
		$5 \times 10^{-17} \text{ s}^{-1}$
	ζ_{H_2} S/H	1.86×10^{-5}
4		
4	G_0 at IF	3.1×10^3
	G_0 at the back side	0.1
	Inclination angle (i)	60°
	Thermal pressure (P_{th})	$2.8 \times 10^8 \text{ K cm}^{-3}$
	$N_H/E(B-V)$	$1.05 \times 10^{22} \text{ cm}^2 \text{ mag}^{-1}$ $5 \times 10^{-17} \text{ s}^{-1}$
	ζ_{H_2}	$5 \times 10^{-17} \text{ s}^{-1}$
	S/H	1.86×10^{-5}
5	G ₀ at IF	3.1×10^5
	G_0 at the back side	0.1
	Inclination angle (i)	60°
	Thermal pressure (P_{th})	$2.8 \times 10^{8} \text{ K cm}^{-3}$
	$N_H/E(B-V)$	$1.05 \times 10^{22} \text{ cm}^2 \text{ mag}^{-1}$
	ζ_{H_2}	$5 \times 10^{-17} \text{ s}^{-1}$
	S/H	1.86×10^{-5}
6	G_0 at IF	3.1×10^4
U		0.1
	G_0 at the back side	60°
	Inclination angle (i)	
	Thermal pressure (P_{th})	$2.8 \times 10^8 \text{ K cm}^{-3}$
	$N_H/E(B-V)$	$1.05 \times 10^{22} \text{ cm}^2 \text{ mag}^{-1}$
	ζ_{H_2}	$5 \times 10^{-16} \text{ s}^{-1}$
	S/H	1.86×10^{-5}
7	G_0 at IF	3.1×10^4
	G_0 at the back side	0.1
	Inclination angle (i)	60°
	Thermal pressure (P_{th})	$2.8 \times 10^{8} \text{ K cm}^{-3}$
	$N_H/E(B-V)$	$1.05 \times 10^{22} \text{ cm}^2 \text{ mag}^{-1}$
	ζ_{H_2}	$5 \times 10^{-17} \text{ s}^{-1}$
	S/H	1.86×10^{-7}
8	G_0 at IF	3.1×10^4
J	G_0 at the back side	0.1 0.1
	Inclination angle (i)	60°
	memanon angle (1)	
		2 0 × 108 IZ1
	Thermal pressure (P_{th})	$2.8 \times 10^8 \text{ K cm}^{-3}$
	Thermal pressure (P_{th}) N _H /E(B-V)	$1.6 \times 10^{22} \text{ cm}^2 \text{ mag}^{-1}$
	Thermal pressure (P_{th})	

¹ The parameters not shown here are the same as in the reference model (see Table 3)